Spatial variation of englacial radar attenuation: Modeling approach and application to the Vostok flowline

Joseph A. MacGregor,[1] Kenichi Matsuoka,[2] Edwin D. Waddington,[3] Dale P. Winebrenner,[3,4] and Frank Pattyn[5]

Received 30 December 2011; revised 7 June 2012; accepted 21 June 2012; published 21 August 2012.

[1] Constraining the spatial variation of englacial radar attenuation is critical for accurate inference of the spatial variation of the englacial and basal properties of ice sheets from radar returned power. Here we evaluate attenuation models that account for spatial variations in ice temperature and chemistry and test them along the flowline that passes through the Vostok ice core site, Antarctica. The simplest model, often used but rarely valid, assumes a uniform attenuation rate everywhere along the flowline, so that total attenuation is proportional to ice thickness. The next simplest model uses spatially varying temperatures predicted by an ice-flow model and assumes uniform chemistry. Additional models account for spatially varying chemistry using englacial stratigraphy. We find that the roundtrip attenuation to the bed can easily differ by 10 dB or more between the uniform attenuation-rate model and models that account for variable ice temperature. Such differences are sufficient to confound the delineation of dry and wet beds. Also including spatial variations in chemistry produces smaller differences (<10 dB), but the magnitude of these differences depends on the relative importance of dry and wet deposition of impurities in the past. Accounting for dry-deposited impurities requires ice-flow modeling and results in larger differences from all other models, which assume uniform chemistry or wet deposition only. These results indicate that modeling the spatial variation of attenuation requires a spatially varying temperature model in order to infer bed conditions from bed returned power accurately, and that both ice core data and radar stratigraphy are also strongly desirable.

Citation: MacGregor, J. A., K. Matsuoka, E. D. Waddington, D. P. Winebrenner, and F. Pattyn (2012), Spatial variation of englacial radar attenuation: Modeling approach and application to the Vostok flowline, *J. Geophys. Res.*, *117*, F03022, doi:10.1029/2011JF002327.

1. Introduction

[2] The current spatial distribution of ice sheet basal conditions is poorly known and has been identified as a major source of uncertainty for predictive ice sheet models [*Alley et al.*, 2005; *Bell*, 2008]. Ice-penetrating radar surveys are one of the primary geophysical tools for the investigation of basal conditions, generally by interpretation of bed reflectivity. The detection of subglacial water using radar is of particular interest [e.g., *Peters et al.*, 2005]. However, the returned power from the bed recorded by radar depends not only on the bed reflectivity, but also on system parameters and englacial losses [e.g., *Matsuoka*, 2011]. Of these losses, the primary unknown is the dielectric attenuation within the ice.

[3] Radar attenuation in ice sheets depends mostly on ice temperature and chemistry [e.g., *MacGregor et al.*, 2007]. Depth-averaged attenuation rates to the bed of polar ice sheets can vary across more than two orders of magnitude (<10 to ~30 dB km^{-1} one way) [e.g., *Jacobel et al.*, 2009, 2010; *Matsuoka et al.*, 2010a, 2012], yet the reflectivity difference between dry and wet beds is only 10–15 dB [e.g., *Peters et al.*, 2005]. Furthermore, many studies have assumed a uniform depth-averaged attenuation rate [e.g., *Bentley et al.*, 1998; *Copland and Sharp*, 2001; *Rippin et al.*, 2004; *Peters et al.*, 2005; *Pattyn et al.*, 2009; *MacGregor et al.*, 2011; *Pettersson et al.*, 2011]. Although in many cases their inferences regarding basal conditions from radar data are qualitatively consistent with glaciological expectations, this assumption limits both the quality of those inferences and the straightforward detection of regions with basal

[1]Institute for Geophysics, University of Texas at Austin, Austin, Texas, USA.
[2]Norwegian Polar Institute, Tromsø, Norway.
[3]Department of Earth and Space Sciences, University of Washington, Seattle, Washington, USA.
[4]Polar Science Center, Applied Physics Lab, University of Washington, Seattle, Washington, USA.
[5]Département des Sciences de la Terre et de l'Environnement, Université Libre de Bruxelles, Brussels, Belgium.

Corresponding author: J. A. MacGregor, Institute for Geophysics, University of Texas at Austin, Austin, TX 78758, USA. (joemac@ig.utexas.edu)

©2012. American Geophysical Union. All Rights Reserved.
0148-0227/12/2011JF002327

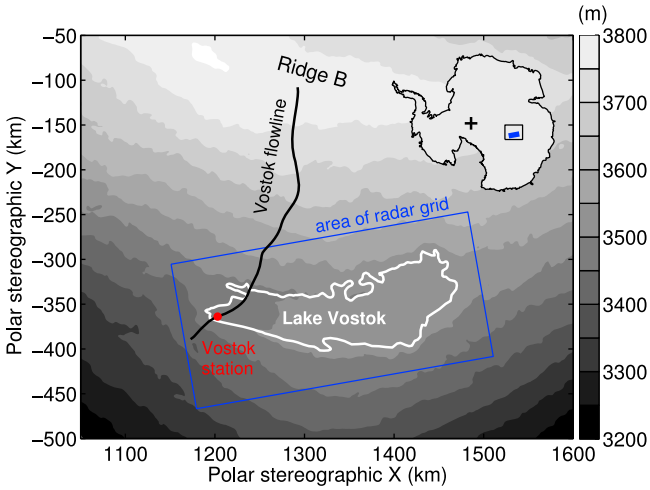

Figure 1. Surface elevation in the Lake Vostok region [*Bamber et al.*, 2009] and location of the flowline that crosses through the Vostok ice core site. The blue solid line outlines the region of the SOAR radar grid [*Studinger et al.*, 2003]. Only the portion of the Vostok flowline within the area of the radar grid is used in this study. Outside of the SOAR grid, the flowline was determined solely using surface elevations; inside the radar grid, it was determined by tracking of structures in the englacial stratigraphy [*Tikku et al.*, 2004]. Inset map shows the location of the study area in Antarctica.

conditions that do not conform with predictions. Both the areal coverage and the quality of radar surveys has increased significantly over the past two decades, but the development of radar-attenuation models has not kept pace with those improvements. A better understanding of the spatial variation of attenuation rates is therefore critical for accurate inference of basal conditions from radar data.

[4] Here we examine attenuation models that account for ice temperature and chemistry and evaluate differences in their predictions along the flowline that passes over subglacial Lake Vostok and through the Vostok ice core site in East Antarctica (Figure 1). We both consider existing models, and develop new models of the horizontal variation of englacial radar attenuation, beginning with the simplest possible model (a uniform attenuation rate) and progressively refining that model using various ice core data (chemistry, density), radar data (englacial stratigraphy) and ice-flow model outputs (temperature, velocity). The Vostok flowline is examined because of the availability of both radar and ice core data, our overarching interest in studying the ice–lake interface of Lake Vostok using radar returned power, and the range of flow regimes that exist along this flowline.

2. Background

2.1. Radar Attenuation

[5] The englacial radar attenuation rate N_a in dB km^{-1} (one-way) is linearly proportional to its high-frequency conductivity σ in μS m^{-1} [*Winebrenner et al.*, 2003]:

$$N_a = \frac{10\log_{10}e}{1000\varepsilon_0\sqrt{\varepsilon'_{ice}}c}\sigma = 0.915\sigma, \quad (1)$$

where e is the natural log base, ε_0 and c are the permittivity and the speed of light in the vacuum, respectively, and ε'_{ice} is the real part of the complex relative permittivity of ice. (Note that *MacGregor et al.* [2007, 2009b] placed the factor of 1000 in the numerator mistakenly.) The above notation and all other notation in this paper are tabulated at the end of this paper. Due to densification, ε'_{ice} increases rapidly with depth within the top ~100 m of an ice sheet, although its horizontal spatial variation is expected to be small (Appendix A), especially compared to σ [e.g., *Matsuoka et al.*, 2010b]. In this study, we assume a uniform value of $\varepsilon'_{ice} = 3.2$.

[6] Ice conductivity depends exponentially on its temperature, depends linearly on its molar concentrations of two soluble impurities (acid and sea-salt chloride), and depends nonlinearly on density (not shown):

$$\sigma = \sigma_{pure}\exp\left[\frac{E_{pure}}{k}\left(\frac{1}{T_r}-\frac{1}{T}\right)\right] + \mu_{H^+}[H^+]\exp\left[\frac{E_{H^+}}{k}\left(\frac{1}{T_r}-\frac{1}{T}\right)\right] + \mu_{ssCl^-}[\text{ss Cl}^-]\exp\left[\frac{E_{ssCl^-}}{k}\left(\frac{1}{T_r}-\frac{1}{T}\right)\right], \quad (2)$$

where k is the Boltzmann constant, T is temperature, and T_r = 251 K is a reference temperature. The magnitudes of these dependencies are represented by the values of six dielectric properties: the pure ice conductivity σ_{pure}, the molar conductivities μ of acid (H^+) and sea-salt chloride (ss Cl^-), and the activation energies E of the pure, H^+ and ss Cl^- components of the conductivity. The values of these dielectric properties (Table 1) were constrained by a recent synthesis of published measurements on laboratory-grown ice and ice cores by *MacGregor et al.* [2007], where further details are available.

[7] Uncertainties in modeled attenuation rates are derived from the uncertainties in the dielectric properties of ice at radio frequencies, temperature, impurity concentrations, and density. Using the mean and standard deviation of published values of those dielectric properties and of typical impurity-concentration data, *MacGregor et al.* [2007] found that the mean relative uncertainty of this conductivity model was 27% (one standard deviation) at Siple Dome, West Antarctica. This uncertainty is inherent to the conductivity model and provides context for the significance of the modeled spatial variation in attenuation rates. In this paper, we focus on the

Table 1. Values of the Dielectric Properties Used in the Ice-Conductivity Model Described by Equation (2)

Symbol	Description	Value
σ_{pure}	Conductivity of pure ice	9.2 μS m^{-1}[a]
μ_{H^+}	Molar conductivity of H^+	3.2 S m^{-1} mol^{-1}
$\mu_{ss\ Cl^-}$[a]	Molar conductivity of ss Cl^-	0.43 S m^{-1} mol^{-1}
E_{pure}	Activation energy of pure ice	0.51 eV[b]
E_{H^+}	Activation energy of H^+	0.20 eV[b]
$E_{ss\ Cl^-}$[a]	Activation energy of ss Cl^-	0.19 eV[b]

[a]Note mistakes in units and symbols in *MacGregor et al.* [2009b, Table 2]: 1. Units for given value of σ_{pure} are in μS m^{-1}, not S m^{-1}. 2. Symbols for the activation energies of H^+ and ss Cl^- ions are $\mu_{ss\ Cl^-}$ and $E_{ss\ Cl^-}$, not μ_{H^+} and E_{H^+}, respectively.
[b]1 eV = 96.5 kJ mol^{-1}.

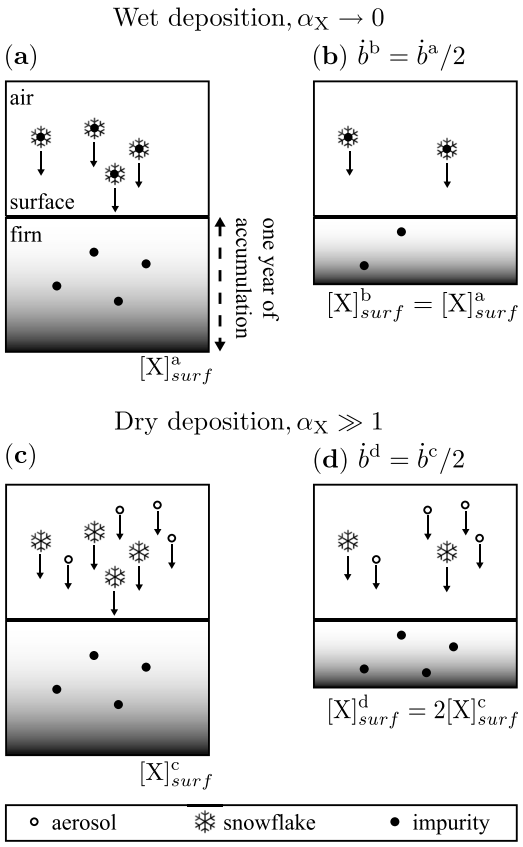

Figure 2. Illustration of the effect of the mode of deposition (wet or dry) on the englacial impurity concentration $[X]_{surf}$, as a function of accumulation rate $\dot{b}$. Superscripts refer to individual panels. The atmospheric impurity concentration is the same for all scenarios, and we note that only atmospheric impurities that are being dry- or wet-deposited are shown. (a, b) Wet deposition only; the accumulation rate in Figure 2b is halved compared to (a), yet $[X]_{surf}$ remains the same. (c, d) Dry deposition only; the accumulation rate in Figure 2d is halved compared to Figure 2c, which causes a doubling of $[X]_{surf}$.

effects of spatially varying ice temperature and chemistry on attenuation, so this uncertainty does not affect our investigation directly. We therefore set aside the issue of uncertainties in the modeled attenuation rates in this study, while clearly recognizing that this uncertainty ultimately affects the interpretation of englacial and basal reflectivity derived from radar data.

[8] Temperatures in ice sheets depend mostly on the downward vertical advection of cold ice from the surface, upward vertical conduction of the geothermal flux from the underlying bed, and downstream horizontal advection of heat. The balance of these heat fluxes typically results in increasing temperatures with depth. Because the conductivity of ice increases exponentially with temperature (equation (2)), attenuation rates also typically increase rapidly with depth [e.g., *MacGregor et al.*, 2007, 2009b], although high surface accumulation rates can produce thick layers of near-isothermal ice and uniform attenuation rates near the surface [*Matsuoka et al.*, 2010b]. Given a temperature field, including spatially varying temperatures in an attenuation-rate model is straightforward. Soluble impurity concentrations in meteoric ice, however, depend on other factors that may vary spatially and temporally (e.g., accumulation rate), which complicates the determination of their spatial variation. Although attenuation rates also depend on density, we assume that the depth profile of density is sufficiently horizontally uniform that spatial density variations are too small to significantly affect modeled attenuation rates (Appendix A).

2.2. Modes of Deposition and Englacial Chemistry

[9] The englacial concentrations of H^+ and ss Cl^- ions depend on their surface fluxes at the time of deposition. Wet and dry deposition are the two primary mechanisms by which impurities are incorporated into meteoric ice; the former occurs during snowfall and the latter is aerosol fall-out. The atmospheric flux f_X of impurity X (H^+ or ss Cl^-) from the atmosphere into the firn is often assumed to be related linearly to its local atmospheric concentration $[X]_{air}$ as [e.g., *Kreutz et al.*, 2000]

$$f_X = (s_X \dot{b} + d_X)[X]_{air}, \tag{3}$$

where $\dot{b}$ is the snow accumulation rate at the time of deposition, s_X is the impurity-specific dimensionless scavenging ratio of that impurity by falling snow, and d_X is the impurity-specific dry deposition speed. The first term represents wet deposition and the second term represents dry deposition. This model neglects fog deposition and other effects, whose contribution to the total impurity flux is minimal along the coast but may be larger farther inland [*Wolff et al.*, 1998]. Post-depositional loss of some species (particularly NO_3^-) can reduce the effective impurity flux into the ice sheet, although here we assume that its effect on f_{H^+} and f_{ssCl^-} is negligible.

[10] The impurity concentration in the near-surface firn is

$$[X]_{surf} = \frac{f_X}{\dot{b}} = \left(s_X + \frac{d_X}{\dot{b}}\right)[X]_{air}. \tag{4}$$

The importance of dry deposition relative to wet deposition is inferred from the ratio of their fluxes:

$$\alpha_X = \frac{d_X}{s_X \dot{b}}. \tag{5}$$

The ratio α_X is species-dependent because both d_X and s_X depend on the particle size of each species in the atmosphere and other atmospheric conditions [e.g., *Alley et al.*, 1995; *Wolff et al.*, 1998]. It varies between ~0.01 on the coast and more than 1 inland [*Legrand*, 1987; *Wolff et al.*, 1998], but measurements of this ratio are challenging and there is much remaining uncertainty regarding both its value for each impurity and its spatial variation.

[11] Figure 2 illustrates the relationships between accumulation rate and englacial impurity concentrations, based on the relative importance of dry and wet deposition. For an impurity whose surface flux is dominated by wet deposition

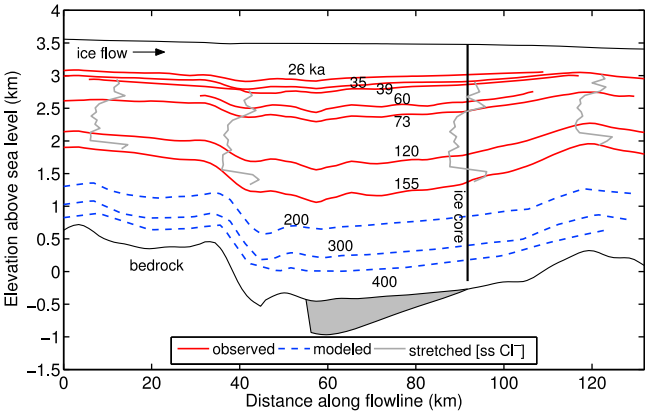

Figure 3. Cross-section of the Vostok flowline showing its main features, and observed and modeled isochrones (ages labeled). The main body of Lake Vostok is shown as gray fill. The stretching process (model $C^{o}_{w,w}$) is also illustrated using the portion of the [ss Cl^{-}] profile between the 35 and 155 ka observed reflectors at selected locations along the flowline, including the ice core profile at Vostok.

($\alpha_X \rightarrow 0$), its englacial impurity concentration is independent of accumulation rate. Conversely, if an impurity's surface flux is dominated by dry deposition ($\alpha_X > 1$), its englacial impurity concentration is inversely proportional to accumulation rate. These contrasting behaviors will affect our implementation of spatially varying chemistry in some of the attenuation-rate models.

2.3. Vostok Flowline Data and Ice-Flow Model

2.3.1. Radar Data and Englacial Stratigraphy

[12] During the 2000–2001 austral summer, the U.S. Support Office for Aerogeophysical Research (SOAR) at The University of Texas at Austin's Institute for Geophysics collected 60-MHz airborne ice-penetrating radar data over the Lake Vostok region in an approximately 150-km by 350-km grid (Figure 1). The radar lines were flown along an orthogonal grid; lines with a roughly east–west orientation had a 7.5-km line spacing, and lines with a roughly north–south orientation had an 11.25- or 22.5-km line spacing. This data set was used to derive ice thickness and bed and surface elevations across the study area [*Studinger et al.*, 2003]. In this study, we examine radar attenuation along a flowline passing through the Vostok ice core site (hereafter Vostok), which was identified using the long-term flow directions determined by *Tikku et al.* [2004] using structure tracking of the englacial stratigraphy. However, none of the SOAR radar transects follows this flowline. *MacGregor et al.* [2009a] interpolated gridded surface and bed elevations and englacial reflector depths picked by *Tikku et al.* [2004] onto the 132-km-long portion of the Vostok flowline that is within the SOAR grid (Figure 1). The maximum distance between the interpolated flowline and the radar data is less than 8 km. Figure 3 shows these interpolated features along the flowlines and their ages, as determined by their interpolated depth at Vostok and its most recent depth–age scale [*Parrenin et al.*, 2004].

[13] To simplify the integration of disparate data into the attenuation-rate model, we define a two-dimensional cross-sectional grid along the flowline. The along-flow horizontal grid spacing is 1.15 km. The vertical grid spacing is one fiftieth of the local ice thickness, meaning that the grid spacing varies along flow between 57 and 79 m, depending on the local ice thickness. The number of vertical layers is arbitrary and was determined based on the trade-off between computational efficiency and the depth resolutions of the ice core chemistry data (<10 m) and the ice-flow model (21 layers with non-uniform thickness).

2.3.2. Ice Core Data

[14] We use ice core chemistry [*Petit et al.*, 1999; *De Angelis et al.*, 2004; M. R. Legrand, personal communication, 2008] and firn-density data [*Lipenkov et al.*, 1997] from the Vostok ice core. These data are identical to those used by *MacGregor et al.* [2009b], where further details are available. We also use the modeled accumulation-rate history and depth–age scale inferred from the ice core data [*Parrenin et al.*, 2004] to constrain impurity-flux histories.

2.3.3. Modeled Ice Temperature and Velocity

[15] For ice temperatures and velocities along the flowline, we interpolated values from an existing three-dimensional (3D) thermomechanical ice-flow model with 5-km horizontal resolution across the entire Antarctic ice sheet and 21 layers in the ice [*Pattyn*, 2010]. The layer thickness decreases with increasing depth in order to better resolve temperature gradients near the bed. Over subglacial lakes and ice streams, the dynamics of this "hybrid" model transition from neglecting horizontal stress gradients to being dominated by them, thus capturing the essential behavior of both ice sheet and ice stream/ice-shelf flow.

[16] Using this flow model, *Pattyn* [2010] conducted 24 experiments using three different accumulation-rate and eight different geothermal flux data sets. These boundary conditions were tuned so that they reproduced the modern ice sheet surface topography, borehole temperatures, and the locations of known subglacial lakes. In our study area, data sources for this calibration include the Vostok borehole-temperature profile, and the extent of Lake Vostok and smaller peripheral subglacial lakes. *Pattyn* [2010] found that modeled englacial temperatures are most sensitive to the geothermal flux. Because attenuation rates depend exponentially on temperature (equation (2)), our attenuation models will be most significantly affected by uncertainty in temperatures near the bed, which is dominated by the geothermal flux uncertainty. For this study, we use ice temperature and velocity fields predicted by *Pattyn* [2010] using an average of the geothermal flux models of *Shapiro and Ritzwoller* [2004] and *Pollard et al.* [2005], and the surface mass balance model of *van de Berg et al.* [2006]. We linearly interpolated ice temperatures and velocities onto our cross-sectional flowline grid (Figure 4).

[17] The modeled flow direction deviates from that determined by tracking the englacial stratigraphy. The mean ratio of the transverse to longitudinal components of the modeled surface velocity is 9.5% when projected onto the flowline derived from *Tikku et al.*'s [2004] flow direction field. This ratio is less than 30% across nearly the entire flowline. Rather than completely relying on the modeled velocities, we choose to use the data-supported flow-direction field of *Tikku et al.*

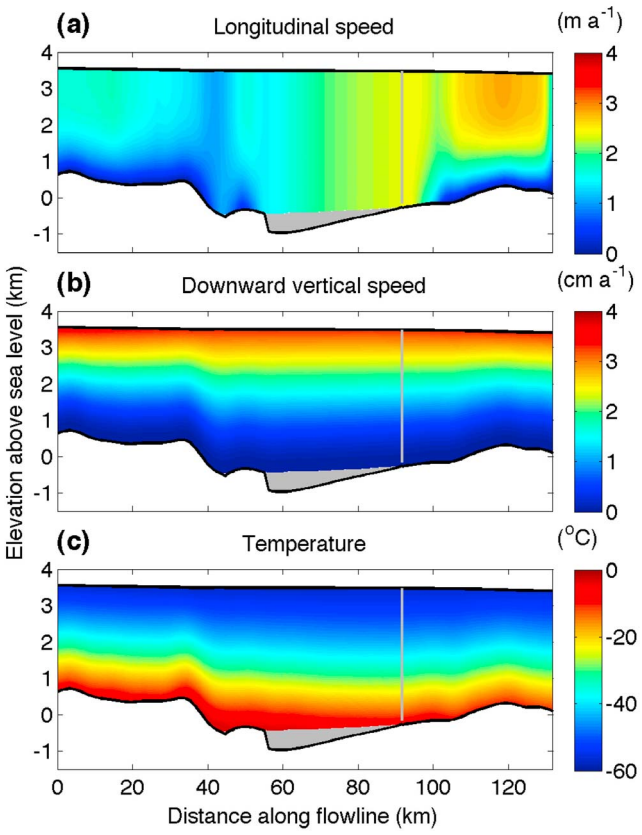

Figure 4. Modeled (a) longitudinal speed, (b) downward vertical speed, and (c) temperature of ice along the Vostok flowline. Solid gray line represents the Vostok ice core.

[2004] and project the modeled velocities onto that flowline. The transverse component of the modeled ice velocities is ignored.

3. Flowline Attenuation Models

[18] We next describe the three spatial models of radar attenuation considered in this study; their distinguishing features are summarized in Table 2, and their application to the Vostok flowline is presented in the following subsections. These models either include or exclude spatial variations in temperature and chemistry. Here we consider models in only two dimensions, because of our focus on the Vostok flowline. However, it is relatively straightforward to extend these models into three dimensions.

3.1. Uniform Temperature and Chemistry (A)

[19] The first spatial model (A) assumes a uniform depth-averaged attenuation rate along the flowline, which is equivalent to assuming that the depth-integrated effect of vertical variations in impurity concentrations and temperature on the depth-averaged attenuation rate does not vary horizontally. Model A is the simplest possible attenuation-rate model and has often been used for studies of bed reflectivity. However, recent work has demonstrated that this model is rarely valid, because of the effect of even modest changes in steady state glaciological conditions on englacial temperatures [*Matsuoka*, 2011]. This model may be acceptable only in areas of an ice sheet where ice thickness has little spatial variation [e.g., *Laird et al.*, 2010], or where the bed is thawed everywhere [e.g., *Langley et al.*, 2011; *Matsuoka*, 2011].

3.2. Spatially Varying Temperature and Uniform Chemistry (B)

[20] This model (B) accounts for spatially varying ice temperature, therefore its attenuation rates vary both horizontally and vertically. However, it also assumes uniform chemistry. It uses the modeled temperatures from the three-dimensional steady state ice-flow model described above. This change from uniform model A is preserved in all subsequent attenuation models (Table 2). The uniform values of $[H^+]$ and [ss Cl^-] can be the depth-averaged values from an ice core along the flowline. Model B is similar to that used by *Carter et al.* [2007] and *Peters et al.* [2007], except that they used a one-dimensional temperature model to vary attenuation rates spatially.

3.3. Spatially Varying Temperature and Chemistry (C)

[21] We next develop a set of models (C) that accounts for the spatial variation of chemistry. For these models, we assume that impurity concentrations in the air over our study area were spatially uniform at any given time in the past. The history of an impurity deposited through time onto an ice sheet can be recovered from ice cores, but spatial patterns of impurity deposition in the past are poorly known. When impurities are wet-deposited, their concentration at the snow surface $[X]_{surf}$ is independent of the surface snow accumulation (equation (4) and Figure 2). In contrast, when impurities are dry-deposited, $[X]_{surf}$ is inversely proportional to the snow accumulation rate. This difference requires different model implementations for dry and wet deposition. We will use purely wet and purely dry deposition as end-members for each impurity in order to bracket the range of modeled attenuation. In both cases, we assume that temporal variation of impurity concentrations in the air $[X]_{air}$ are fully represented by the ice core records, that s_X and d_X remain constant in time and uniform in space, and that the impurity concentrations of a unit volume of ice deposited at the surface do not change over time as that volume is strained by ice flow.

Table 2. Main Features of the Spatially Varying Attenuation-Rate Models[a]

Model	Temperature	Impurity Concentrations
Ice core	Variable[b]	Ice core
A	Uniform	Uniform
B	Variable	Uniform
$C^o_{d,d}$, $C^o_{d,w}$, $C^o_{w,w}$, $C^o_{w,d}$	Variable	Stretched using observed stratigraphy only
$C^{o,m}_{d,d}$, $C^{o,m}_{d,w}$, $C^{o,m}_{w,w}$, $C^{o,m}_{w,d}$	Variable	Stretched using observed and modeled stratigraphy

[a]For the different versions of model C, the superscript designates whether the version uses observed stratigraphy only ("o") or both observed and modeled stratigraphy ("o,m") to determine the spatial variation of chemistry. The subscript designates the assumed mode of deposition (dry, "d," or wet "w") for each impurity (H^+, then ss Cl^-).

[b]Temperatures from three-dimensional ice-flow model, not the borehole-temperature profile.

3.3.1. Wet Deposition Case

[22] In the case of wet deposition, the impurity concentration is independent of the surface accumulation rate (Figure 2). If a given impurity is entirely wet-deposited ($\alpha_X \rightarrow 0$), then its concentration $[X]_{wet}(x, A)$ is independent of the layer thickness:

$$[X]_{wet}(x, A) = [X](x_{core}, A), \tag{6}$$

where x is the along-flow position and A is the age when the ice was originally deposited as snow. Radar reflectors (assumed to be isochrones) can be dated at an ice core site and tracked along-flow. These data constitute a set of along-flow depth profiles $z_i(x, A_i)$. Each pair of consecutive isochrones brackets a layer of variable thickness. The thickness of the layer varies across the study area because the accumulation rate varies in space and time, and each volume of ice between these reflectors has experienced a different strain rate history along its path [e.g., *Waddington et al.*, 2007]. This "stretching" approach is essentially the same as that employed by *Carter et al.* [2009] to model attenuation, although the methodology and its implicit assumptions are described more fully here. Specifically, here we clarify the mode of deposition (wet) that is implied by the use of equation (6), and that the stretching is best described in terms of ice age, which is not necessarily linear between dated isochrones. As we discuss below, this method is valid only when all impurities are wet-deposited.

3.3.2. Dry Deposition Case

[23] If an impurity is entirely dry-deposited ($\alpha_X \gg 1$), then $[X]_{surf}$ is proportional to $[X]_{air}/\dot{b}$ (Figures 2c and 2d). Because the impurity concentration is invariant within the initial unit volume of ice, the englacial impurity concentration $[X]_{dry}(x, A)$ within the strained volume is also inversely proportional to its accumulation rate at the time of deposition $\dot{b}(x^0(x, A), A)$:

$$[X]_{dry}(x, A) = \frac{\dot{b}(x^0(x_{core}, A), A)}{\dot{b}(x^0(x, A), A)} [X](x_{core}, A). \tag{7}$$

The accumulation rate depends on the age and origin x^0 of a given particle that is currently at position x. We note that the dual assumptions of dry deposition and uniform impurity concentrations in the air are equivalent to assuming that the flux of that impurity to the surface is uniform (equation (3)).

[24] Depth profiles of impurity concentrations at ice core sites are available, so the remaining challenge in the determination of $[X]_{dry}(x, A)$ is to estimate the accumulation-rate ratio in equation (7). However, an ice core can provide information only about accumulation rates at the points of origin when the ice recovered in the core was originally deposited at the surface. Furthermore, there is currently no reliable or generally accepted method to extract spatial and temporal accumulation rate patterns from ice core chemistry alone [*Waddington et al.*, 2005]. Independent estimates of the accumulation-rate history can be derived for the surface points of origin of ice now at the ice core site, based on ice core isotope chemistry and detailed transient ice-flow modeling [e.g., *Parrenin et al.*, 2001, 2004]. Annual layer thicknesses provide the best information about along-flow accumulation rates over time, although poorly known strain due to ice flow is a complication.

[25] Below we present an approach for estimating the accumulation-rate ratio using radar-detected isochrones and simple ice-flow modeling. Layer shapes in a steady state ice sheet can closely resemble the layer shapes in a transient ice sheet [e.g., *Waddington et al.*, 2005]; the major difference between them is the distribution of ice age as a function of depth. To address this issue, first we use the radar layers to constrain a simple one-dimensional (1D) steady state ice-flow model and infer the spatial patterns of accumulation rate for the time interval bracketed by each radar layer. Second, we estimate the temporal pattern of accumulation by comparing those accumulation rates inferred with the steady state 1D model against the more detailed modeled accumulation-rate history inferred from the ice core using transient ice-flow models. Finally, using the 1D model, we calculate the shapes of undetected isochrones within each radar layer. These synthetic sub-layers can be dated at the ice core and are used to provide greater temporal resolution on the inferred accumulation-rate history along the flowline.

[26] Accumulation rate and ice thickness are the primary controls on the thickness of any layer at depth. Accumulation rate at the origin site x^0 determines the initial thickness of annual layers, and thickness of the entire ice column influences layer thinning with depth. Inference of accumulation-rate patterns from isochrones can be treated at three levels of complexity, depending on layer depths and on the spatial variability of strain encountered by particles along their flow paths. Here we use a procedure of intermediate complexity, called the Local Layer Approximation (LLA) [*Waddington et al.*, 2007], in which we account for vertical strain associated with ice flow, but we assume that horizontal variations of accumulation rate and ice thickness are small along the particle paths. Appendix B summarizes this approach and describes how to assess the suitability of the LLA for any particular layer. Solving the 3D deep-layer problem along the Vostok flowline is beyond the scope of this paper. Here we use the LLA for our calculations, with the caveat of reduced confidence in the inferred values of $[X]_{dry}$ as compared to $[X]_{wet}$.

[27] Appendix B also describes how we can use the radar isochrones to infer along-flow profiles of effective steady state accumulation rate $\dot{b}^i_{eff}(x)$ and effective ice sheet thickness $H^i_{eff}(x)$ for each radar layer bounded by two isochrones ($z^i_{top}(x)$ and $z^i_{bot}(x)$). In our LLA model for the ith radar layer, these two parameters ($\dot{b}^i_{eff}(x)$ and $H^i_{eff}(x)$) place both the top and bottom isochrones at the correct depths with the correct ages. Note that the LLA is equivalent to a 1D model, so that $x^0(x, A) = x$ for all points x, including x_{core}. These profiles of $\dot{b}^i_{eff}(x)$ suitably represent the spatial pattern of accumulation rate within each time interval bracketed by the two isochrones.

[28] Knowing $\dot{b}^i_{eff}(x)$ and $H^i_{eff}(x)$ for each radar layer, we can then determine the along-flow profile $z(x, A)$ of any isochrone within that layer (Appendix B):

$$\frac{z(x, A)}{H^i_{eff}(x)} = 1 - \exp\left(-\frac{\dot{b}^i_{eff}(x) A}{H^i_{eff}(x)}\right). \tag{8}$$

At any location x, the depth $z(x, A)$ is consistent with the logarithmic strain pattern expected in a flowing steady state ice sheet, and because it is sandwiched between the two well-constrained isochrones, any error in the dating will be minimal (apart from influences of transient past accumulation rate, which we can deal with only approximately here). The measured impurity concentrations in the ice core [X] (x_{core}, A) can be followed along these synthetic isochrones to provide finer resolution on temporal accumulation-rate variations.

[29] Because the steady LLA model does not capture transient accumulation-rate variations or the detailed strain history along different particle paths, different layers at the same point x along the flowline can have different values of $\dot{b}_{eff}$ and H_{eff}. From existing estimates of the accumulation-rate history for particles in the ice core $\dot{b}(x^0(x_{core}, A), A)$, we calculate the mean accumulation rate for any time interval (A_{bot}, A_{top}):

$$\bar{\dot{b}}_{core}(x_{core}, A_{bot}, A_{top}) = \frac{\int_{A_{bot}(x_{core})}^{A_{top}(x_{core})} \dot{b}\left(x^0(x_{core}, t), t\right) dt}{A_{bot} - A_{top}}, \quad (9)$$

where the bounding ages A_{bot} and A_{top} can either be those of radar-detected isochrones or undetected isochrones computed from equation (8).

[30] For the ith layer, $\dot{b}^i_{eff}(x_{core})$, which is an ice-flow-weighted average of the accumulation rate since the isochrones were deposited, will not necessarily agree with $\bar{\dot{b}}^i_{core}$, which is the average accumulation rate only during the period bracketed by those isochrones. We define the dimensionless ratio γ^i between these values as

$$\gamma^i = \frac{\bar{\dot{b}}^i(x_{core}, A_{bot}, A_{top})}{\dot{b}^i_{eff}(x_{core})} = \frac{\bar{\dot{b}}^i_{core}}{\dot{b}^i_{eff}(x_{core})}. \quad (10)$$

When accumulation rate is controlled by temperature through the Clausius–Clapeyron relation, as it is on the East Antarctic ice sheet, and when climatic temperature changes are spatially uniform, then temporal accumulation-rate variations throughout a region can be described by a spatially uniform multiplicative time series applied to a spatial accumulation-rate pattern, rather than by a spatially uniform additive time series [e.g., *Parrenin et al.*, 2004]. Therefore, we can use γ^i to rescale our entire spatial pattern of accumulation rate $\dot{b}^i_{eff}(x)$ within the period bracketed by A_{bot} and A_{top} using the actual average accumulation rate at the one location where it is known, i.e., the ice core site:

$$\bar{\dot{b}}(x, A_{bot}, A_{top}) = \gamma^i \dot{b}^i_{eff}(x). \quad (11)$$

Moreover, the same spatial function $\dot{b}^i_{eff}(x)$ can be used to estimate the actual accumulation rate pattern that produced any thinner sub-layer bounded by isochrones within the ith layer; this sub-layer can be as thin as a single annual layer. Equation (9) provides the mean accumulation rate during the period of deposition at the ice core site. A formulation analogous to equation (10) for the correction within this sub-layer can also be determined. However, when all that is needed is the ratio of accumulation rates to estimate $[X]_{dry}(x, A)$, γ^i and the sub-layer's ratio will cancel out, reducing equation (7) to

$$[X]_{dry}(x, A) = \frac{\dot{b}^i_{eff}(x_{core})}{\dot{b}^i_{eff}(x)} [X](x_{core}, A). \quad (12)$$

3.3.3. Mixed Cases

[31] Because the ratio of dry to wet deposition (α, equation (5)) remains unknown in most cases, and H^+ and ss Cl^- may be deposited by different mechanisms, here we examine all four end-member cases (dry or wet for H^+ or ss Cl^-, or both). We label the models using subscripts to designate the modes of deposition for H^+ and then for ss Cl^-, e.g., $C_{d,w}$ represents the model that treats H^+ as dry-deposited and ss Cl^- as wet-deposited.

[32] Equations (6) and (14) show how impurity concentrations can be estimated along-flow by weighting ice core data and mapping them along isochronous layering in the ice, depending on the mode of deposition. However, it is common to observe few or no radar reflectors at great depths because total englacial signal loss increases with depth, and because ice-flow-induced shear increases with proximity to the bed and strains layers whose interfaces might otherwise be visible [e.g., *Fujita et al.*, 1999; *Matsuoka et al.*, 2003; *Jacobson and Waddington*, 2004; *Drews et al.*, 2009]. Along our Vostok flowline, radar reflectors that were tracked over the majority of the SOAR grid are located in the upper half of the ice sheet (Figure 3). We treat the deepest layer, whose upper surface is the deepest observed radar reflection and whose lower surface is the bed, as a single thick layer when estimating the spatial variation of chemistry for attenuation modeling. This problem motivates the use of modeled isochrones at greater depths. To produce these isochrones, we integrated the modeled velocities for the study area from *Pattyn* [2010] along particle paths [e.g., *Waddington et al.*, 2007]. When only observed isochrones are used we label the model with the superscript "o" (C^o); when both observed and modeled isochrones are used, we label the model with the superscript "o,m" ($C^{o,m}$).

4. Application to the Vostok Flowline

4.1. Attenuation-Rate Profiles at Vostok

[33] We first compare depth profiles of attenuation rate at Vostok estimated by the three spatial models and our previous attenuation-rate profile for Vostok modeled using borehole temperature, chemistry and density data [*MacGregor et al.*, 2009b] (Figure 5a). That "ice-core" model was adjusted for the glaciological conditions at Vostok, and we use the same adjustments here. First, ice temperatures are below the eutectic point of HNO_3 (−43°C) in the upper one-third of the ice column, so we do not include the conductivity contribution from this acid in ice below its eutectic point, where it is not expected to conduct electrolytically. Second, the conductivity contribution from impurities is also ignored within the accreted ice above the southern end of Lake Vostok, where large impurity concentrations (e.g., $[Cl^-] > 30\ \mu M$) are observed but are not likely to increase conductivity [*MacGregor et al.*, 2009b]. The ice core model uses the full-resolution ice core-chemistry data and the

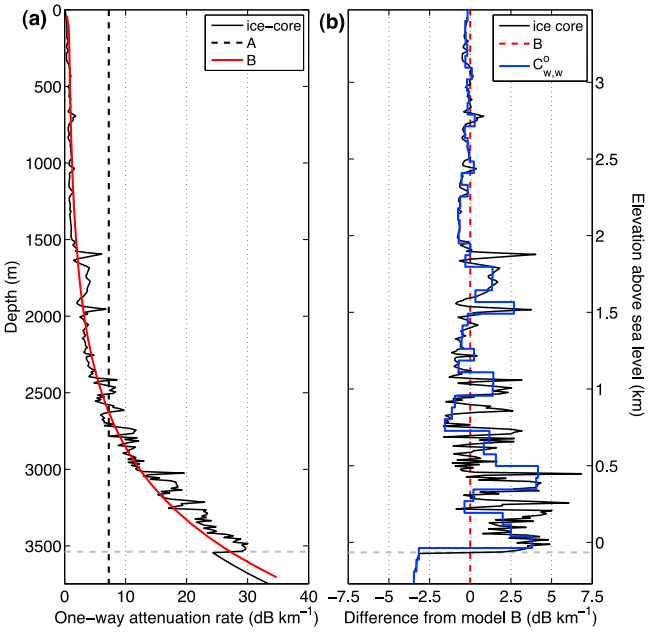

Figure 5. (a) Depth profiles of one-way attenuation rate at Vostok for the attenuation-rate models A (uniform), B (variable temperature, uniform chemistry), and the ice core model. (b) Differences from model B for the ice core model and model C (variable temperature and chemistry). At the ice core site, all versions of model C are identical. The horizontal gray dashed line represents the boundary between meteoric and accreted ice at Vostok.

temperature profile at Vostok from the ice-flow model. This ice core model differs from that presented by *MacGregor et al.* [2009b], who used the borehole-temperature profile, in order to simplify comparison of the different spatially varying attenuation-rate models. Attenuation rates predicted with this ice core model are lower than those presented by *MacGregor et al.* [2009b], because the ice-flow model predicts a lower-magnitude basal temperature gradient at Vostok, leading to lower temperatures at large depths there. The ice core model's depth-averaged value (7.2 dB km^{-1}) is the value assigned to the uniform attenuation-rate model (A).

[34] Figure 5a shows the modeled one-way attenuation-rate profiles for models A and B, which assume uniform impurity concentrations, along with the ice core model. Specifically, both models use the mean impurity concentrations in the meteoric ice at Vostok (0.5 μM and 2.0 μM for [H^+] and [ss Cl^-], respectively) as the uniform values. The differences between these models (Table 3) illustrate the limitations of assuming a uniform depth-averaged attenuation rate when calculating depth profiles of reflectivity, due to changing temperature and chemistry. For the mean impurity concentrations in the meteoric ice at Vostok, the attenuation-rate contribution from pure ice dominates at temperatures above $\sim -40°C$. This temperature occurs at depths below 1700 m at Vostok, and the pure ice component contributes 81% of the total attenuation to the ice bottom in this deeper ice. Nevertheless, the attenuation-rate contribution from impurities is important in the upper half of the ice sheet and influences its depth-averaged value [*MacGregor et al.*, 2007, 2009b].

Table 3. Key Metrics for the Attenuation-Rate Models

Model	Depth-Averaged Attenuation Rate at Vostok (dB km^{-1})	Fraction of Flowline With Total Attenuation Difference From Model A Greater Than ±10 dB
Ice core	7.2	N/A
A	7.2	N/A
B	7.0	0.29
$C^o_{d,d}$	7.1[a]	0.34
$C^o_{d,w}$	7.1[a]	0.32
$C^o_{w,w}$	7.1[a]	0.30
$C^o_{w,d}$	7.1[a]	0.29
$C^{o,m}_{d,d}$	7.1[a]	0.28
$C^{o,m}_{d,w}$	7.1[a]	0.29
$C^{o,m}_{w,w}$	7.1[a]	0.28
$C^{o,m}_{w,d}$	7.1[a]	0.28

[a]The value at the ice core site is the same for all versions of model C.

[35] Figure 5b shows the difference in attenuation rate at Vostok between the models that vary both temperature and chemistry (ice core, $C^o_{w,w}$) and that which varies temperature but not chemistry (B). The layer thicknesses used by model C to stretch the impurity-concentration profiles are normalized by their values at the ice core site, so all versions of model C are simply subsampled versions of the adjusted ice core model there. The difference in depth-averaged attenuation-rate between the ice core model and model C at Vostok is only 0.1 dB km^{-1} (Table 3), which suggests that averaging the ice core chemistry data over intervals of tens of meters does not significantly hinder attenuation-rate modeling relative to using maximum resolution available.

4.2. Flowline Attenuation Rates

[36] Figure 6 shows the spatial variation of attenuation rates along the Vostok flowline predicted by the non-uniform temperature/uniform chemistry model (B). Attenuation rates are low (<10 dB km^{-1}) in the upper ~2.5 km of the ice column across the entire flowline, and rapidly increase within 500–800 m of the bed. This bottom layer has a non-uniform thickness along the flowline because of the effects of both varying ice thickness and the presence of Lake Vostok on modeled temperatures. Figure 7 shows the differences

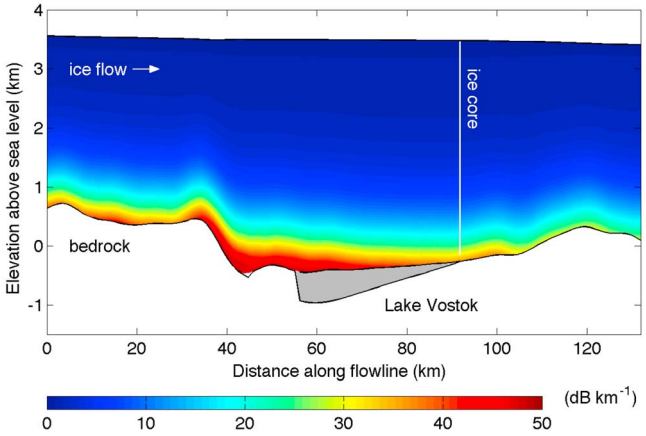

Figure 6. Attenuation rates (one-way) along the Vostok flowline for model B (variable temperature, uniform chemistry).

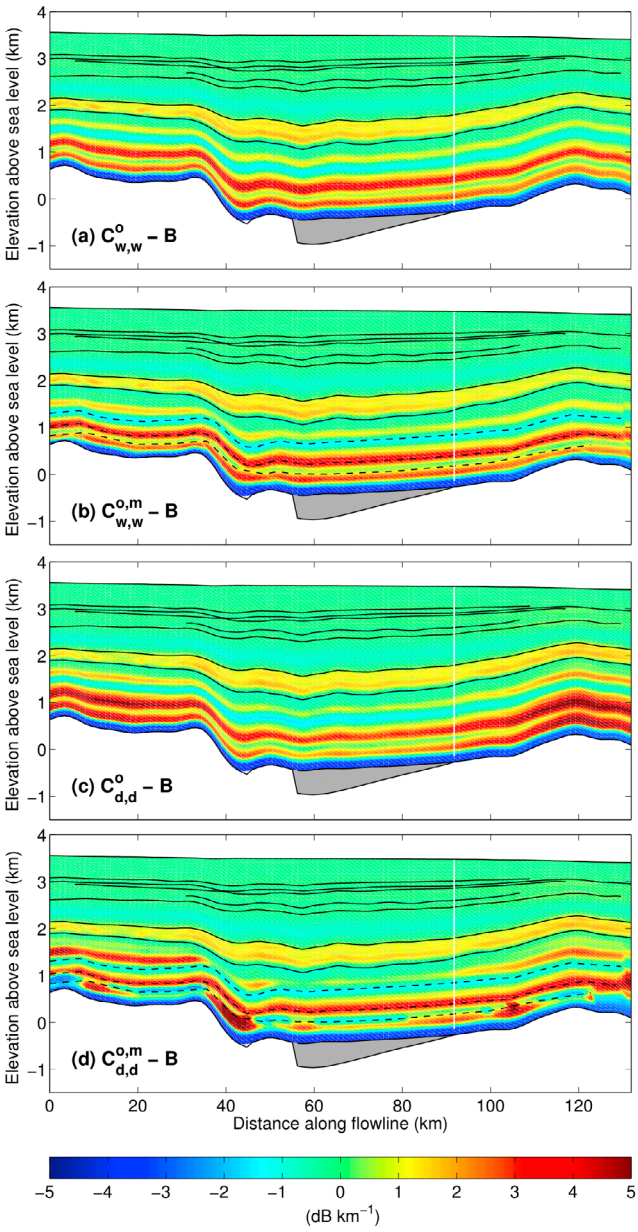

Figure 7. (a–d) Differences between attenuation-rate models that have both variable temperature and chemistry (C) and model B (variable temperature, uniform chemistry; Figure 6). The band of negative differences close to the bed is a consequence of the zeroed impurity concentrations assumed for accreted ice, in terms of their contribution to radar attenuation [*MacGregor et al.*, 2009b].

between model C, which includes the spatial variation of chemistry, and model B. The inclusion of non-uniform chemistry stretched by the observed and modeled isochrones results in non-uniform layers of lower and higher attenuation rates, particularly in the deeper half of the ice sheet. At Vostok, impurity concentrations are often higher than their depth-averaged values deeper in the ice sheet, partly explaining the differences between model B and the four versions of model C shown in Figure 7 ($C^{o}_{w,w}$, $C^{o,m}_{w,w}$, $C^{o}_{d,d}$, and $C^{o,m}_{d,d}$). The layer of negative differences between models B and C immediately above the bed is due the zeroed impurity concentrations in the accreted ice, although we do not anticipate lake-accreted ice upstream of Lake Vostok. The true attenuation-rate behavior of the accreted ice will vary depending on the (unknown) relationship between its wildly varying impurity concentrations and bulk high-frequency conductivity. As expected, the differences are largest for models $C^{o}_{d,d}$ and $C^{o,m}_{d,d}$, because dry-deposited impurity concentrations are more sensitive to layer-thickness variations and strain rate modeling (equations (6) and (12)).

[37] Figure 8 shows the depth-averaged attenuation rates and roundtrip attenuation along the Vostok flowline. The maximum difference in the depth-averaged attenuation rates between the non-uniform models and the uniform model A (4.1 dB km^{-1}) is about four times the maximum difference between the non-uniform models (1.1 dB km^{-1}). For example, stretching impurity-concentration profiles using the observed isochrones increases the depth-averaged

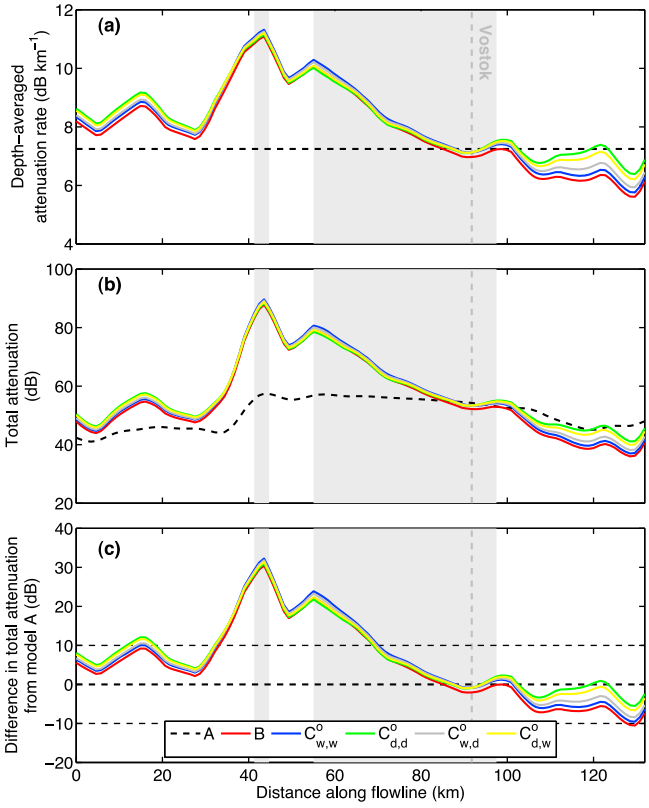

Figure 8. (a) Depth-averaged attenuation rates and (b) total round-trip attenuation from the surface to the bed for the attenuation-rate models A, B, $C^{o}_{d,d}$, $C^{o}_{w,w}$, $C^{o}_{w,d}$, and $C^{o}_{d,w}$ along the Vostok flowline. (c) Difference in total roundtrip attenuation to the bed between the non-uniform models and the uniform model (A) along the Vostok flowline. Model A (dashed black horizontal line at 0 dB) has zero difference from itself; thin gray dashed lines at ±10 dB represent the nominal threshold for discriminating between dry and wet beds. Negative (positive) values of this difference imply that model A overestimates (underestimates) the total attenuation. Gray fill shows where the flowlines crosses over the main part of Lake Vostok and a shallow bay.

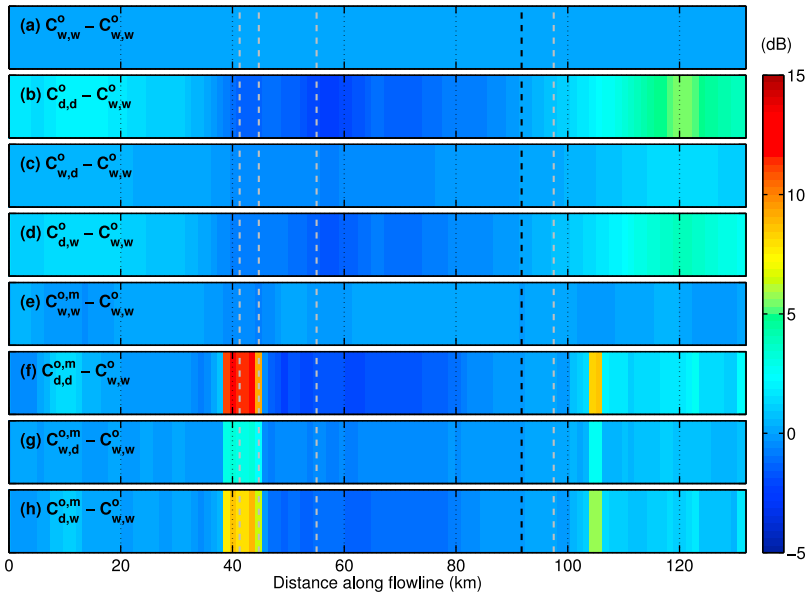

Figure 9. (a–h) Differences in the total (round-trip) attenuation between all C models and $C^{o}_{w,w}$. Black dashed line represents the location of Vostok, and vertical gray dashed lines show the edges of Lake Vostok and the shallow bay.

attenuation rates along the Vostok flowline by only 0.2 ± 0.0 dB km^{-1} (mean difference between models B and $C^{o}_{w,w}$). Impurity concentrations greater than their depth-averaged values cause larger increases in attenuation rate at greater depths, because of the combination of the nonlinear dependence of attenuation rate on temperature (equation (2)) and higher temperatures near the bed (Figure 4c).

[38] At Vostok, the depth of the oldest observed radar reflector is 2210 m, which is 56% of the ice thickness there. The observed stratigraphy can therefore usefully stretch the chemistry over only about half of the ice thickness along the flowline studied here. Using the modeled steady state velocities, we produced three isochrones (Figure 3) that are 200-, 300-, and 400-ka old, and then included them in the stretching process for the four versions of model $C^{o,m}$. This age range lies between the age of the oldest observed isochrone (155 ka) and the age of the oldest ice above the accreted basal ice layers at Vostok (~420 ka) [*Parrenin et al.*, 2004]. Including the three modeled isochrones (200-, 300- and 400-ka) has a negligible effect on depth-averaged attenuation rates; the mean difference between models that do and do not include the modeled isochrones is less than 0.1 dB km^{-1}. These modeled isochrones generally conform to the bed but occasionally deviate substantially where the bed topography or basal boundary condition is changing substantially (e.g., km 0–10, 35–45, 100–108), so they are likely due to limitations of the ice-flow model's resolution. These deviations can result in large differences (up to 15 dB) from model B that do not match the expected smooth variation of attenuation rates along-flow, but the differences are generally less than 5 dB (Figure 9). Despite limitations inherent to the modeling of isochrones using steady state velocities, our results suggest that at least for the Vostok flowline only observed reflectors are necessary when predicting the spatial variation of chemistry for the purpose of attenuation-rate modeling.

[39] In terms of the total roundtrip attenuation, the differences between the uniform and non-uniform models are largest where horizontal gradients in ice thickness and temperature are also largest (Figure 8c). There, these differences often exceed 10 dB (Table 3), which is the nominal threshold for distinguishing between dry and wet beds [e.g., *Peters et al.*, 2005]. These differences tend to be smaller (<10 dB) over the downstream half of Lake Vostok (~km 75–97), where ice-thickness changes are smallest. The uniform model (A) underestimates the total attenuation upstream of Vostok, which would lead to underestimated bed reflectivity.

[40] To better distinguish the different versions of model C, Figure 9 shows their differences in total (roundtrip) attenuation from $C^{o}_{w,w}$. These differences are largest upstream (km 38–44), where the layers are thinner than at Vostok. Model $C^{o,m}_{d,d}$ is the most sensitive to layer-thickness variations, due to the larger depth variability of the older modeled isochrones near the bed, where attenuation rates are also increasing rapidly. The differences between $C^{o}_{w,d}/C^{o,m}_{w,d}$ and $C^{o}_{w,w}$ are typically less than half of those between $C^{o}_{d,w}/C^{o,m}_{d,w}$ and $C^{o}_{w,w}$, because the contribution of ss Cl^{-} to attenuation is ~7 times smaller than that of H^{+} (Table 1). These differences show that understanding each impurity's mode of deposition is important to the stretching attenuation-rate models (C) shown here, even compared to the broader spatial variability of chemistry inferred from the englacial stratigraphy.

5. Discussion

5.1. Uniform Versus Non-uniform Attenuation-Rate Models

[41] Our results further emphasize that the common assumption of a uniform depth-averaged attenuation rate (model A) is often inadequate, even in relatively slow-moving

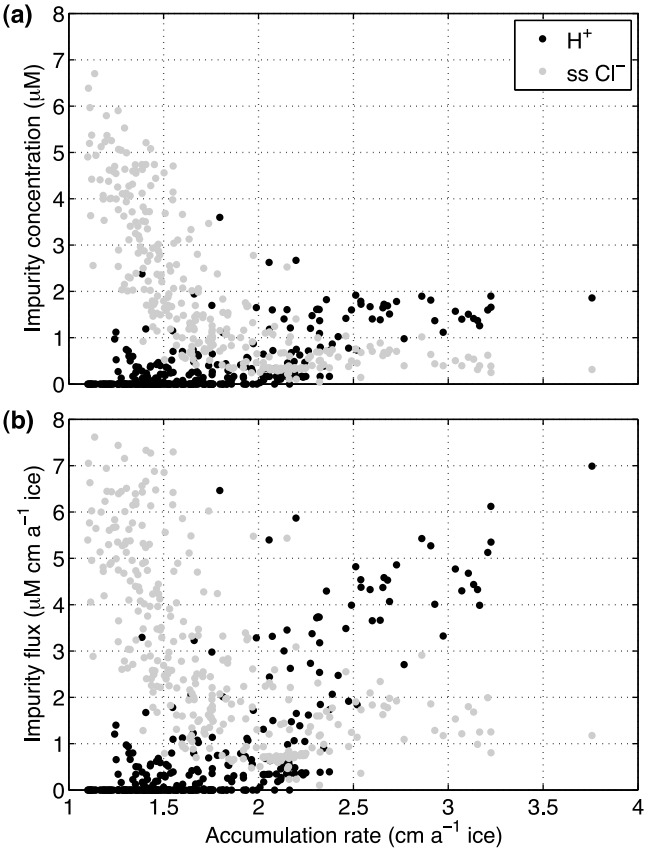

Figure 10. Relationships between accumulation rate, (a) impurity concentration, and (b) impurity flux for the Vostok ice core.

ice, where horizontal gradients in the ice properties that affect radar attenuation can still be non-negligible. Errors in the roundtrip attenuation can easily exceed 10 dB, thus confounding the first-order goal of any study of the returned power from the bed, i.e., distinguishing between wet and dry beds [e.g., *Jacobel et al.*, 2009]. It is clear from our results that the inclusion of spatially varying temperatures in an attenuation model has the largest effect on the spatial variation of attenuation (e.g., Figure 8). The inclusion of spatially varying chemistry has a secondary but non-negligible effect on modeled attenuation rates, although it may be of primary importance in coastal regions with larger climatic gradients [*Corr et al.*, 1993]. For the Vostok flowline, stretching impurity-concentration profiles using the englacial stratigraphy does not significantly change the portion of the flowline where the total attenuation difference exceeds 10 dB (Figure 8c and Table 3). Model $C^{o}_{w,w}$ has the largest range of attenuation rates (5.8–11.3 dB km^{-1}), and these values are significantly different from that used for uniform model A (7.2 dB km^{-1}).

5.2. Implementation of Spatial Variation of Chemistry

[42] Figure 9 shows that the effect of spatial variation of chemistry on modeled attenuation is dependent on the local flow regime, our ability to resolve ice-flow changes between these regimes, and the assumed mode of deposition. The magnitude of the modeled variations can reach 15 dB across distances of less than 2 km (i.e., $C^{o,m}_{d,d}$), which we consider unlikely and hence more representative of limitations in our modeling approach than of the true variability of radar attenuation along the flowline. However, the extreme variations do speak to an important limitation of any approach to modeling attenuation. Where the ice-flow regime changes suddenly, our ability to predict attenuation is potentially limited, and hence also our ability to infer englacial and subglacial properties from radar data [e.g., *MacGregor et al.*, 2011]. Finally, where the nature of impurity deposition is poorly constrained, our ability to resolve such features is further limited.

5.3. Vostok-Specific Attenuation-Rate Modeling

[43] The eight versions of model C represent all possible end-members in terms of the dominant mode of deposition. We now consider which model is most appropriate for each impurity at Vostok. There, [ss Cl$^-$] is inversely proportional to accumulation rate, whereas [H$^+$] is weakly proportional to accumulation rate (Figure 10a). The observed scatter is typical of such relationships [*Alley et al.*, 1995; *Wolff et al.*, 1998; *Kreutz et al.*, 2000], and we note that the relationship between impurity flux and accumulation rate (equation (4) and Figure 10b) has an inherent bias to produce a positive correlation [*Alley et al.*, 1995]. These relationships suggest that, at Vostok, dry deposition is the dominant contributor to $f_{\mathrm{ssCl^-}}$, whereas the dry deposition contribution to $f_{\mathrm{H^+}}$ is small. These two impurities represent opposing depositional end-members ($\alpha_{\mathrm{H^+}} \rightarrow 0$ and $\alpha_{\mathrm{ssCl^-}} \geq 1$), suggesting the following impurity-specific simplifications to equation (4):

$$[\mathrm{H^+}]_{surf} = s_{\mathrm{H^+}}[\mathrm{H^+}]_{air}, \tag{13}$$

$$[\mathrm{ss\ Cl^-}]_{surf} = \frac{d_{\mathrm{ssCl^-}}}{\dot{b}}[\mathrm{ss\ Cl^-}]_{air}. \tag{14}$$

We note that neither of these ions is deposited independent of other impurities; H$^+$ ions likely fallout as acids, and ss Cl$^-$ ions are expected to be part of sea-salt aerosols. These relationships are also affected by climatic changes across glacial–interglacial cycles other than accumulation-rate variability, but in this study we are more concerned with the form of the empirical relationship between englacial impurity concentrations and accumulation rate.

[44] Based on these contrasting relationships, we consider models $C^{o}_{d,w}$ and $C^{o,m}_{d,w}$ to be the C models most likely to be representative of the pattern of radar attenuation along the Vostok flowline. Compared to other pairs of C models, this pair of models is relatively sensitive to layer-thickness variations (Figure 9) because H$^+$ is treated as dry-deposited, and it is the dominant impurity in attenuation models. Downstream of Lake Vostok, this model pair is closer to model A than all other non-uniform models except $C^{o}_{d,d}$ and $C^{o,m}_{d,d}$.

5.4. Improving Attenuation-Rate Models

[45] The large spatial variation of modeled radar attenuation predicted along the Vostok flowline demonstrates that the conventional method of assuming a uniform attenuation rate is invalid along this flowline and probably elsewhere. Previously, *Matsuoka* [2011] demonstrated that, even if accumulation rate and geothermal fluxes do not vary, ice-

thickness variability alone induces significant spatial variation in depth-averaged attenuation rates. That study used a one-dimensional steady state temperature model to demonstrate this pitfall, and our present study, using more sophisticated temperature modeling, demonstrates that this pitfall also arises for a more realistic case in East Antarctica.

[46] The Greenland and Antarctic ice sheets are increasingly well surveyed by radar using both densely spaced grids (e.g., the SOAR radar data used in this study; NASA's Operation IceBridge) and along flowlines [e.g., *Matsuoka et al.*, 2003]. Radar surveying is also often part of the site-selection process for ice cores, so radar transects crossing through ice core sites are commonly available. Many additional areas of interest therefore have radar stratigraphy that could be used to implement model C and constrain the spatial variation of chemistry [e.g., *Carter et al.*, 2009].

[47] An alternative approach to estimating the spatial variation of chemistry along a flowline is to reverse-track particle paths from within the flowline grid (x, z) to determine their point of origin on the surface and age (x^0, A). Using those values, the accumulation rate at the time of deposition $\dot{b}\,(x^0(x,\ A),\ A)$ could then be inferred and equation (7) could be used to calculate $[\mathrm{X}]_{dry}(x,\ A)$. This approach requires the assumption that impurity flux is spatially uniform, so if the ice-flow history is perfectly modeled, then this alternative model should be equivalent to model $\mathrm{C}_{d,d}^{o,m}$. We experimented with this approach but found that a steady state velocity field was insufficient to reliably estimate (x^0, A) along the Vostok flowline. Although this approach is currently limited by the use of a steady state ice-flow model, its method (tracking the depositional history of impurities) is promising and should be considered by future models of the spatial variation of attenuation. Its methodology could be improved using a transient thermomechanical ice sheet model that keeps track of non-diffusive ice properties such as impurity concentrations [e.g., *Clarke et al.*, 2005], rather than the reversed particle paths from a steady state velocity field.

[48] Because our results show that temperature models are critical for estimating the spatial variation of attenuation, improvements to temperature models will lead most directly to improved attenuation estimates. Thermomechanical ice sheet models are becoming increasingly sophisticated in their treatment of different ice-flow regimes (e.g., ice divides versus ice streams) and spatially varying bed properties such as geothermal flux [e.g., *Pattyn*, 2010]. Although most of these models do not explicitly include all subglacial processes that can affect the basal temperature and its condition (wet/dry), they offer increasingly detailed predictions of ice sheet temperatures that can be partially validated by borehole-temperature profiles [e.g., *Pattyn*, 2010] or other, indirect means of detecting subglacial water, such as surface-elevation change detection [e.g., *Fricker et al.*, 2007]. The transient nature of this temperature field is a complication that should also be considered. Ice sheet-scale thermomechanical modeling depends strongly on available gridded data sets, so future improvements in the latter will also improve attenuation-rate modeling, e.g., ice-thickness or surface-velocity grids [e.g., *Rignot et al.*, 2011]. Propagation of data uncertainty (or missing data) into thermomechanical model outputs [e.g., *Pattyn*, 2010; *Larour et al.*, 2012] will also contribute to better evaluation of uncertainty in radar-attenuation models.

[49] We have emphasized the value of validated thermomechanical modeling in attenuation-rate modeling, and conclude by commenting on the circularity of this argument. If a thermomechanical model were to predict the thermal state of an ice sheet perfectly (including its bed), then radar interpretation of basal conditions and hence attenuation-rate modeling would be unnecessary. In the absence such an ideal temperature model, we must use available temperature models in our attenuation-rate modeling to detect regions where, for example, bed reflectivity is significantly higher (likely indicating the presence of water) than that implied by the modeled thermal state of the bed. In turn, temperature models can be refined to reflect inferences from the radar observations. This sequence emphasizes the co-dependence of these two important types of glaciological studies (ice sheet modeling and ice-penetrating radar surveys) in resolving the englacial and subglacial nature of ice sheets.

6. Conclusions

[50] We found that, for investigations of returned power from radar surveys of ice sheets, the commonly applied model of a uniform depth-averaged attenuation rate is inadequate for distinguishing dry and wet beds (by up to a third of the length Vostok flowline examined here, as compared to more sophisticated models) (Figure 8 and Table 3). Ice temperatures are the most critical element of a spatially varying radar-attenuation model, and radar stratigraphy can be readily used to refine the impurity-concentration field for such spatial models. Accounting for the spatial variation of impurity concentrations requires detailed knowledge of the atmospheric impurity-concentration, accumulation-rate, and ice-flow histories along the flowline of interest, but these values can be inferred from proxy data and models. The spatiotemporal variation of impurity fluxes to the ice sheet surface by dry and wet deposition also affects englacial impurity concentrations and hence attenuation rates, but the effect of uncertainty in the mode of deposition on attenuation is secondary to that of temperature. Interpretation of englacial and bed returned power must consider the spatial variation of radar attenuation [e.g., *Carter et al.*, 2007, 2009; *Matsuoka*, 2011; *Matsuoka et al.*, 2012], and interpretations of apparent spatial variations of englacial and bed reflectivity by earlier studies that assumed a uniform attenuation rate may well require revisiting [e.g., *Rippin et al.*, 2004; *Peters et al.*, 2005; *MacGregor et al.*, 2011]. We conclude that, for radar surveys of ice sheets that aim to investigate the spatial variation of returned power (e.g., subglacial lake detection), a minimally adequate radar-attenuation model must include the spatial variation of temperatures and, where available, ice core-derived impurity concentrations that are extended horizontally using radar stratigraphy.

Appendix A: Spatial Variation of Density and Radar Attenuation

[51] In this study, we assume that the ice core density profile at Vostok is valid along the entire modeled flowline. However, spatial variations in density may affect our spatial models of radar attenuation. Here we evaluate the possible effect of spatial variations in density by using two end-member densification models to model the attenuation-rate

profile at Vostok. We use the empirical densification model of *Herron and Langway* [1980], whose primary model parameters are the surface density, the mean annual surface temperature and accumulation rate. Typical values for a coastal Antarctic site are 350 kg m^{-3}, −20°C and 350 kg m^{-2} a^{-1}, respectively, and 300 kg m^{-3}, −50°C and 20 kg m^{-2} a^{-1} for an East Antarctic site similar to Vostok [*Herron and Langway*, 1980]. Using either modeled density profile, the modeled depth-averaged radar attenuation rate at Vostok differs from that modeled using the measured density profile by less than 0.01 dB km^{-1}, which is much less than the formal uncertainty of the attenuation model at typical ice sheet temperatures. We therefore conclude that spatial variations in density are not an important concern when modeling the spatial variation of radar attenuation.

Appendix B: Inference of Accumulation Rates From Isochrones

[52] *Waddington et al.* [2007] described how to infer accumulation rate from isochrones at three levels of complexity. For a shallow isochrone at depth z with age A that has experienced very little cumulative dynamic strain associated with ice flow, the average accumulation rate can be estimated simply as

$$\dot{b} = \frac{z}{A}. \tag{B1}$$

This "shallow layer approximation" is valid only when $z/H \ll 1$, i.e., in only the upper few percent of the ice sheet thickness H.

[53] Older and deeper layers have undergone significant strain due to ice flow. Near the center of an ice sheet, such as the Lake Vostok region, that strain is generally horizontal stretching and vertical thinning. When the accumulation rate and the vertical velocity profile are horizontally invariant in the region traversed by the particles that form the isochrones, we can infer the accumulation rate by correcting for the local vertical strain with a 1D ice-flow model. *Waddington et al.* [2007] termed this approximation the "local layer approximation" (LLA). A common further simplification with the LLA is the assumption that the vertical strain rate is invariant in the upper layers of an ice sheet [e.g., *Dansgaard and Johnsen*, 1969]. The vertical velocity can then be written as

$$w(x,z) = \frac{dz}{dt} = \dot{b}(x)\left(1 - \frac{z(x)}{H_{eff}(x)}\right), \tag{B2}$$

where H_{eff} is the effective depth at which the linear near-surface velocity $w(x, z)$ would project to zero. For example, in the original formulation of *Dansgaard and Johnsen* [1969], $H_{eff} = H - (h/2)$, where h is the so-called kink height; typically $h/H \approx 0.2$ at flank sites, so $H_{eff} = 0.9\ H$. With this LLA model, an improved estimate of accumulation rate is

$$\dot{b} \approx -\ln\left(1 - \frac{z_{layer}}{H_{eff}}\right)\frac{H_{eff}}{A}. \tag{B3}$$

A non-dimensional number D determines whether the LLA is applicable [*Waddington et al.*, 2007]. Defining L_{path} to be the characteristic length of a particle trajectory, $L_H = |H/(dH/dx)|$ to be the distance over which ice thickness changes significantly, and $L_{\dot{b}} = \left|\dot{b}/\left(d\dot{b}/dx\right)\right|$ to be the distance over which accumulation rate changes significantly, D can be expressed as

$$D = L_{path}\left(\frac{1}{L_{\dot{b}}} + \frac{1}{L_H}\right). \tag{B4}$$

When $D \ll 1$, particles do not move large distances across strong accumulation-rate or ice-thickness gradients, therefore the LLA can be applicable for layers at depths spanning a large fraction of H_{eff}. However, for deep layers where $D \approx 1$ or greater, the LLA is not applicable, and the accumulation-rate pattern must be inferred by solving a formal inverse problem in which the data are the dated isochrones and the forward algorithm is an ice-flow model that calculates isochrones by solving for velocity fields and tracking particle paths [e.g., *Waddington et al.*, 2007; *MacGregor et al.*, 2009a]. Instead, here we use the LLA to infer accumulation rates from dated isochrones, while recognizing that as a consequence of its assumptions the inferred impurity concentrations $[X]_{dry}(x, A)$ using equation (12) deep in the ice sheet are more uncertain.

[54] Integrating equation (B2) from the surface to a given depth z yields

$$\frac{z(x,A)}{H_{eff}(x)} = 1 - \exp\left(-\frac{\dot{b}(x)A}{H_{eff}(x)}\right). \tag{B5}$$

Recognizing that

$$\dot{\varepsilon}_{eff} = \dot{b}_{eff}/H_{eff} \tag{B6}$$

is a characteristic strain rate under the assumption that $w(x, z)$ varies linearly with z, and solving for H_{eff}, we rewrite equation (B5) as

$$H_{eff}(x) = \frac{z(x,A)}{1 - \exp\left(-A\dot{\varepsilon}_{eff}(x)\right)}. \tag{B7}$$

Each radar layer is bounded by two isochrones whose depths z and ages A are known. We further assume that the two unknowns H_{eff} and $\dot{\varepsilon}_{eff}$ are uniform with depth within each layer, although they may vary with along-flow position x. Our goal is now to find the values of H_{eff} and $\dot{b}_{eff}$ that are consistent with the physics of ice flow and that place the two bounding isochrones at the correct depths ($z_{top}(x)$ and $z_{bot}(x)$) and ages (A_{top} and A_{bot}) in an LLA model.

[55] To find $H^i_{eff}(x)$ and $\dot{\varepsilon}^i_{eff}(x)$ for the ith layer, we write two instances of equation (B7) at the layer's top and bottom isochrones, respectively, and eliminate $H^i_{eff}(x)$, to yield a single equation for $\dot{\varepsilon}^i_{eff}(x)$:

$$z^i_{top}(x)\left(1 - \exp\left(-A_{bot}\dot{\varepsilon}^i_{eff}\right)\right) - z^i_{bot}(x)\left(1 - \exp\left(-A_{top}\dot{\varepsilon}^i_{eff}\right)\right) = 0. \tag{B8}$$

We solve equation (B8) numerically for $\dot{\varepsilon}^i_{eff}(x)$ by Newton's method. Substitution of $\dot{\varepsilon}^i_{eff}(x)$ into equation (B7) then yields $H^i_{eff}(x)$, and the effective accumulation rate $\dot{b}^i_{eff}(x)$ for each layer is then derived from equation (B6).

[56] Because the LLA vertical velocity model (equation (B2)) may not capture the exact strain rate history along different particle paths, different layers at location x may have different effective ice sheet thicknesses and effective steady accumulation rates. Furthermore, $\dot{b}^{i}_{eff}(x)$ is the value that puts the top and bottom interfaces of that layer at the correct depths in a local, one-dimensional steady state model, so it should be considered only an effective or characteristic value for the current layer, rather than the actual value at the time and place that the ice was deposited at the surface.

[57] Having determined $H^{i}_{eff}(x)$ and $\dot{b}^{i}_{eff}(x)$ for each layer, we then use equation (B5) to determine the along-flow depth profile $z(x, A)$ of any isochrone of age $A_{top} < A < A_{bot}$ within the current layer, i.e.,

$$z(x,A) = H^{i}_{eff}(x)\left(1 - \exp\left(-\frac{\dot{b}^{i}_{eff}(x)A}{H^{i}_{eff}(x)}\right)\right). \qquad \text{(B9)}$$

This depth profile is consistent with the logarithmic strain rate patterns predicted for a steady ice sheet, and because it is sandwiched between the two well-constrained interfaces at the top and bottom of the layer, any error in the dating will be minimal, apart from the influence of transient past accumulation rates, with which we can deal with only approximately here. The measured impurity concentrations in the ice core $[X](x_{core}, A)$ can be followed along these additional modeled isochrones to provide finer resolution on modeled attenuation rates.

Notation

N_a radar attenuation rate (equation (1))
ε_0 permittivity of the vacuum (8.854×10^{-12} F m^{-1})
ε'_{ice} real part of the complex relative permittivity of pure ice (3.2)
c speed of light in the vacuum (2.998×10^{8} m s^{-1})
σ high-frequency conductivity (equation (2))
E_{pure}, E_{H^+}, $E_{ss\ Cl^-}$ activation energies of the conductivity contributions from pure ice, H^+, and ss Cl^-, respectively
μ_{H^+}, $\mu_{ss\ Cl^-}$ molar conductivities of H^+ and ss Cl^- impurities, respectively
k Boltzmann constant (1.381×10^{-23} J K^{-1})
T Temperature
T_r reference temperature (251 K)
f impurity flux to the surface (equation (3))
s scavenging ratio
d dry deposition speed
$\dot{b}$ accumulation rate
α ratio of dry to wet impurity fluxes (equation (5))
x horizontal position along flowline
z depth
H ice thickness
A ice age
$x^0(x, A)$ along-flow position of surface origin of a particle of age A that is currently at position x
x_{core} along-flow position of the ice core site
$[X]_{wet}$, $[X]_{dry}$ impurity concentration assuming only wet or dry deposition, respectively (equations (6) and (7))
$[X](x_{core}, A)$ time series of impurity concentrations recorded by the ice core at x_{core}
$\dot{b}(x^0(x, A), A)$ accumulation rate at the location and time of deposition
$\dot{b}^{i}_{eff}$, H^{i}_{eff}, $\dot{\epsilon}^{i}_{eff}$ effective steady state accumulation rate, ice thickness, and strain rate for the ith layer, respectively
z_{top}, z_{bot} depth of top and bottom isochrones bounding a layer, respectively
A_{top}, A_{bot} age of top and bottom isochrones bounding a layer, respectively
$\bar{\dot{b}}(x_{core}, A_{bot}, A_{top})$ accumulation rate for particles now at x_{core} averaged over the period bounded by A_{bot} and A_{top} (equation (9))
γ^{i} ratio between $\bar{\dot{b}}(x_{core}, A_{bot}, A_{top})$ and $\dot{b}^{i}_{eff}(x_{core})$ for the ith layer (equation (10))
w vertical velocity (equation (B2))
h kink height above bed
D LLA suitability index (equation (B4))
L_{path}, $L_{\dot{b}}$, L_H characteristic length scales of particle trajectories, accumulation-rate changes, and ice-thickness changes, respectively (equation (B4))

[58] **Acknowledgments.** The U.S. National Science Foundation supported this work at the University of Washington (ANT 0538674). The Applied Physics Laboratory at the University of Washington provided a research fellowship for J. MacGregor. We thank M. Studinger for providing the flow field, the former SOAR at The University of Texas at Austin for collection of the radar data, J.-R Petit, M. de Angelis and M. Legrand for providing the ice core-chemistry data, and V. Lipenkov for the density data. We thank the editor (B. Hubbard), R. Bingham, and two anonymous reviewers for comments that improved the manuscript.

References

Alley, R. B., R. C. Finkel, K. Nishizumi, S. Anandakrishnan, C. A. Shuman, G. Mershon, G. A. Zielinski, and P. A. Mayewski (1995), Changes in continental and sea-salt atmospheric loadings in central Greenland during the most recent deglaciation: Model-based estimates, *J. Glaciol.*, *41*(139), 503–514.

Alley, R. B., P. U. Clark, P. Huybrechts, and I. Joughin (2005), Ice-sheet and sea-level changes, *Science*, *310*, 456–460, doi:10.1126/science.1114613.

Bamber, J. L., J. L. Gomez-Dans, and J. A. Griggs (2009), A new 1 km digital elevation model of the Antarctic derived from combined satellite radar and laser data–Part 1: Data and methods, *Cryosphere*, *3*, 101–111, doi:10.5194/tc-3-101-2009.

Bell, R. E. (2008), The role of subglacial water in ice-sheet mass balance, *Nat. Geosci.*, *1*(5), 297–304, doi:10.1038/ngeo186.

Bentley, C. R., N. Lord, and C. Liu (1998), Radar reflections reveal a wet bed beneath stagnant Ice Stream C and a frozen bed beneath ridge BC, West Antarctica, *J. Glaciol.*, *44*(146), 149–156.

Carter, S. P., D. D. Blankenship, M. E. Peters, D. A. Young, J. W. Holt, and D. L. Morse (2007), Radar-based subglacial lake classification in Antarctica, *Geochem. Geophys. Geosyst.*, *8*, Q03016, doi:10.1029/2006GC001408.

Carter, S. P., D. D. Blankenship, D. A. Young, and J. W. Holt (2009), Using radar data to identify the sources and distribution of subglacial water in radar-sounding data: Application to Dome C, East Antarctica, *J. Glaciol.*, *55*(194), 1025–1040, doi:10.3189/002214309790794931.

Clarke, G. K. C., N. Lhomme, and S. J. Marshall (2005), Tracer transport in the Greenland ice sheet: Three-dimensional isotopic stratigraphy, *Quat. Sci. Rev.*, *24*, 155–171, doi:10.1016/j.quascirev.2004.08.021.

Copland, L., and M. Sharp (2001), Mapping thermal and hydrological conditions beneath a polythermal glacier with radio-echo sounding, *J. Glaciol.*, *47*(157), 232–242, doi:10.3189/172756501781832377.

Corr, H. F. J., J. C. Moore, and K. W. Nicholls (1993), Radar absorption due to impurities in Antarctic ice, *Geophys. Res. Lett.*, *20*(11), 1071–1074, doi:10.1029/93GL01395.

Dansgaard, W., and S. J. Johnsen (1969), A flow model and a time scale for the ice core from Camp Century, Greenland, *J. Glaciol.*, *8*(53), 215–233.

De Angelis, M., J.-R. Petit, J. Savarino, R. Souchez, and M. H. Thiemens (2004), Contributions of an ancient evaporitic-type reservoir to subglacial Lake Vostok chemistry, *Earth Planet. Sci. Lett.*, *222*, 751–765, doi:10.1016/j.epsl.2004.03.023.

Drews, R., O. Eisen, I. Weikusat, S. Kipfstuhl, A. Lambrecht, D. Steinhage, F. Wilhelms, and H. Miller (2009), Layer disturbances and radio-echo free zone in ice sheets, *Cryosphere*, *3*, 195–203, doi:10.5194/tc-3-195-2009.

Fricker, H. A., T. Scambos, R. Bindschadler, and L. Padman (2007), An active subglacial water system in West Antarctica mapped from space, *Science*, *315*, 1544–1548, doi:10.1126/science.1136897.

Fujita, S., S. Uratsuka, T. Furukawa, S. Mae, Y. Fujii, and O. Watanabe (1999), Nature of radio echo layering in the Antarctic ice sheet detected by a two-frequency experiment, *J. Geophys. Res.*, *104*(B6), 13,013–13,024, doi:10.1029/1999JB900034.

Herron, M. M., and C. C. Langway Jr. (1980), Firn densification: An empirical model, *J. Glaciol.*, *25*(93), 373–385.

Jacobel, R. W., B. C. Welch, D. Osterhouse, R. Pettersson, and J. A. MacGregor (2009), Spatial variation of radar-derived basal conditions on Kamb Ice Stream, West Antarctica, *Ann. Glaciol.*, *50*(51), 10–16, doi:10.3189/172756409789097504.

Jacobel, R. W., K. E. Lapo, J. R. Stamp, B. W. Youngblood, B. C. Welch, and J. L. Bamber (2010), A comparison of bed reflectivity and ice velocity in East Antarctica, *Cyrosphere*, *4*, 447–452, doi:10.5194/tc-4-447-2010.

Jacobson, H. P., and E. D. Waddington (2004), Recumbent folding in ice sheets: A core-referential study, *J. Glaciol.*, *50*(168), 3–16, doi:10.3189/172756504781830204.

Kreutz, K. J., P. A. Mayewski, L. D. Meeker, M. S. Twickler, and S. I. Whitlow (2000), The effect of spatial and temporal accumulation rate variability in West Antarctica on soluble ion deposition, *Geophys. Res. Lett.*, *27*(16), 2517–2520, doi:10.1029/2000GL011499.

Laird, C. M., W. A. Blake, K. Matsuoka, H. Conway, C. T. Allen, C. J. Leuschen, and S. Gogineni (2010), Deep ice stratigraphy and basal conditions in central West Antarctica revealed by coherent radar, *IEEE Geosci. Remote Sens. Lett.*, *7*(2), 246–250, doi:10.1109/LGRS.2009.2032304.

Langley, K., J. Kohler, K. Matsuoka, A. Sinisalo, T. Scambos, T. Neumann, A. Muto, J.-G. Winther, and M. Albert (2011), Recovery Lakes, East Antarctica: Radar assessment of sub-glacial water extent, *Geophys. Res. Lett.*, *38*, L05501, doi:10.1029/2010GL046094.

Larour, E., J. Schiermeier, E. Rignot, H. Seroussi, M. Morlighem, and J. Paden (2012), Sensitivity of Pine Island Glacier ice flow using ISSM and DAKOTA, *J. Geophys. Res.*, *117*, F02009, doi:10.1029/2011JF002146.

Legrand, M. (1987), Chemistry of Antarctic snow and ice, *J. Phys.*, *48*(3), 77–86.

Lipenkov, V. Y., A. N. Salamatin, and P. Duval (1997), Bubbly ice densification in ice sheets: II. Applications, *J. Glaciol.*, *43*(145), 397–407.

MacGregor, J. A., D. P. Winebrenner, H. Conway, K. Matsuoka, P. A. Mayewski, and G. D. Clow (2007), Modeling englacial radar attenuation at Siple Dome, West Antarctica, using ice chemistry and temperature data, *J. Geophys. Res.*, *112*, F03008, doi:10.1029/2006JF000717.

MacGregor, J. A., K. Matsuoka, M. R. Koutnik, E. D. Waddington, M. Studinger, and D. P. Winebrenner (2009a), Millennially averaged accumulation rates for the Vostok Subglacial Lake region inferred from deep internal layers, *Ann. Glaciol.*, *50*(51), 25–34, doi:10.3189/172756409789097441.

MacGregor, J. A., K. Matsuoka, and M. Studinger (2009b), Radar detection of accreted ice over Lake Vostok, Antarctica, *Earth Planet. Sci. Lett.*, *282*, 222–233, doi:10.1016/j.epsl.2009.03.018.

MacGregor, J. A., S. Anandakrishnan, G. A. Catania, and D. P. Winebrenner (2011), The grounding zone of the Ross Ice Shelf, from ice-penetrating radar, *J. Glaciol.*, *57*(205), 917–928, doi:10.3189/002214311798043780.

Matsuoka, K. (2011), Pitfalls in radar diagnosis of ice-sheet bed conditions: Lessons from englacial attenuation models, *Geophys. Res. Lett.*, *38*, L05505, doi:10.1029/2010GL046205.

Matsuoka, K., T. Furukawa, S. Fujita, H. Maeno, S. Uratsuka, R. Naruse, and O. Watanabe (2003), Crystal orientation fabrics within the Antarctic ice sheet revealed by a multipolarization plane and dual-frequency radar survey, *J. Geophys. Res.*, *108*(B10), 2499, doi:10.1029/2003JB002425.

Matsuoka, K., J. A. MacGregor, and F. Pattyn (2010a), Using englacial radar attenuation to better diagnose the subglacial environment: A review, in *Proceedings of the 13th International Conference on Ground Penetrating Radar*, pp. 482–486, IEEE, Washington, D. C., doi:10.1109/ICGPR.2010.5550161.

Matsuoka, K., D. L. Morse, and C. F. Raymond (2010b), Estimating englacial radar attenuation using depth profiles of returned power, central West Antarctica, *J. Geophys. Res.*, *115*, F02012, doi:10.1029/2009JF001496.

Matsuoka, K., F. Pattyn, D. Callens, and H. Conway (2012), Radar characterization of the basal interface across the grounding line of an ice-rise promontory in East Antarctica, *Ann. Glaciol.*, *53*(60), 29–34, doi:10.3189/2012AoG60A106.

Parrenin, F., J. Jouzel, C. Waelbroeck, C. Ritz, and J.-M. Barnola (2001), Dating the Vostok ice core by an inverse method, *J. Geophys. Res.*, *106*(D23), 31,837–31,851, doi:10.1029/2001JD900245.

Parrenin, F., F. Rémy, C. Ritz, M. J. Siegert, and J. Jouzel (2004), New modeling of the Vostok ice flow line and implication for the glaciological chronology of the Vostok ice core, *J. Geophys. Res.*, *109*, D20102, doi:10.1029/2004JD004561.

Pattyn, F. (2010), Antarctic subglacial conditions inferred from a hybrid ice sheet/ice stream model, *Earth Planet. Sci. Lett.*, *295*(3–4), 451–461, doi:10.1016/j.epsl.2010.04.025.

Pattyn, F., C. Delcourt, D. Samyn, B. de Smedt, and M. Nolan (2009), Bed properties and hydrological conditions underneath McCall Glacier, Alaska, USA, *Ann. Glaciol.*, *50*(51), 80–84, doi:10.3189/172756409789097559.

Peters, M. E., D. D. Blankenship, and D. L. Morse (2005), Analysis techniques for coherent airborne radar sounding: Application to West Antarctic ice streams, *J. Geophys. Res.*, *110*, B06303, doi:10.1029/2004JB003222.

Peters, M. E., D. D. Blankenship, S. P. Carter, S. D. Kempf, and J. W. Holt (2007), Along-track focusing of airborne radar sounding data From West Antarctica for improving basal reflection analysis and layer detection, *IEEE Trans. Geosci. Remote Sens.*, *45*(9), 2725–2736, doi:10.1109/TGRS.2007.897416.

Petit, J.-R., et al. (1999), Climate and atmospheric history of the past 420,000 years from the Vostok ice core, Antarctica, *Nature*, *399*, 429–436, doi:10.1038/20859.

Pettersson, R., P. Christoffersen, J. A. Dowdeswell, V. A. Pohjola, A. Hubbard, and T. Strozzi (2011), Ice thickness and basal conditions of Vestfonna Ice Camp, eastern Svalbard, *Geogr. Ann., Ser. A*, *93*(4), 311–322, doi:10.1111/j.1468-0459.2011.00438.x.

Pollard, D., R. M. DeConto, and A. N. Nyblade (2005), Sensitivity of Cenozoic Antarctic ice sheet variations to geothermal flux, *Global Planet. Change*, *49*(1–2), 63–74, doi:10.1016/j.gloplacha.2005.05.003.

Rignot, E., J. Mouginot, and B. Scheuchl (2011), Ice flow of the Antarctic ice sheet, *Science*, *333*(6048), 1427–1430, doi:10.1126/science.1208336.

Rippin, D. M., J. L. Bamber, M. J. Siegert, D. G. Vaughan, and H. F. J. Corr (2004), The role of ice thickness and bed properties on ice dynamics of the enhanced-flow tributaries of Bailey Ice Stream and Slessor Glacier, Antarctica, *Ann. Glaciol.*, *39*, 366–372, doi:10.3189/172756404781814375.

Shapiro, N. M., and M. H. Ritzwoller (2004), Inferring surface heat flux distributions guided by a global seismic model: Particular application to Antarctica, *Earth Planet. Sci. Lett.*, *223*(1–2), 213–224, doi:10.1016/j.epsl.2004.04.011.

Studinger, M., et al. (2003), Ice cover, landscape setting, and geological framework of Lake Vostok, East Antarctica, *Earth Planet. Sci. Lett.*, *205*, 195–210, doi:10.1016/S0012-821X(02)01041-5.

Tikku, A. A., R. E. Bell, M. Studinger, and G. K. C. Clarke (2004), Ice flow field over Lake Vostok, East Antarctica, inferred by structure tracking, *Earth Planet. Sci. Lett.*, *227*, 249–261, doi:10.1016/j.epsl.2004.09.021.

van de Berg, W. J., M. R. van den Broeke, C. H. Reijmer, and E. van Meijgaard (2006), Reassessment of Antarctic surface mass balance using calibrated output of a regional atmospheric climate model, *J. Geophys. Res.*, *111*, D11104, doi:10.1029/2005JD006495.

Waddington, E. D., H. Conway, E. J. Steig, R. B. Alley, E. J. Brook, K. C. Taylor, and J. W. C. White (2005), Decoding the dipstick: Thickness of Siple Dome, West Antarctica at the Last Glacial Maximum, *Geology*, *33*(4), 281–284, doi:10.1130/G21165.1.

Waddington, E. D., T. A. Neumann, M. R. Koutnik, H.-P. Marshall, and D. L. Morse (2007), Inference of accumulation-rate patterns from deep layers in glaciers and ice sheets, *J. Glaciol.*, *53*(183), 694–712, doi:10.3189/002214307784409351.

Winebrenner, D. P., B. E. Smith, G. A. Catania, H. B. Conway, and C. F. Raymond (2003), Radio-frequency attenuation beneath Siple Dome, West Antarctica, from wide-angle and profiling radar observations, *Ann. Glaciol.*, *37*, 226–232, doi:10.3189/172756403781815483.

Wolff, E. W., J. S. Hall, R. Mulvaney, E. C. Pasteur, D. Wagenbach, and M. Legrand (1998), Relationship between chemistry of air, fresh snow and firn cores for aerosol species in coastal Antarctica, *J. Geophys. Res.*, *103*(D9), 11,057–11,070, doi:10.1029/97JD02613.